

# Spherical Convolutional Neural Networks: Stability to Perturbations in $SO(3)$

Zhan Gao, Fernando Gama, and Alejandro Ribeiro

**Abstract**—Spherical signals are useful mathematical models for data arising in many 3-D applications such as LIDAR images, panorama cameras, and optical scanners. Successful processing of spherical signals entails architectures capable of exploiting their inherent data structure. In particular, spherical convolutional neural networks (Spherical CNNs) have shown promising performance in shape analysis and object recognition. In this paper, we focus on analyzing the properties that Spherical CNNs exhibit as they pertain to the rotational structure present in spherical signals. More specifically, we prove that they are equivariant to rotations and stable to rotation diffeomorphisms. These two properties illustrate how Spherical CNNs exploit the rotational structure of spherical signals, thus offering good generalization and faster learning. We corroborate these properties through controlled numerical experiments.

**Index Terms**—Spherical convolutional neural networks, rotation equivariance, diffeomorphism stability

## I. INTRODUCTION

Modern image-acquisition technologies such as light detection and ranging (LIDAR) [1], panorama cameras [2] and optical scanners [3] obtain data that can be conveniently modeled as located on a spherical surface in a 3-D space [4]. Thus, applications like object classification in computer vision [5], panoramic video processing in self-driving cars [6] and 3-D surface reconstruction in medical imaging [7] require information processing architectures capable of handling the characteristics of 3-D data.

Spherical signals offer a mathematical description for data located on surfaces of the 3-D space [8], [9]. They essentially assign a scalar (or vector) value to each point in a spherical surface. Processing such signals in a successful manner entails exploiting the structure given by the surface. In particular, we are concerned about exploiting the rotational structure of spherical signals [10], [11].

The rotational structure can be captured by means of the rotation group. This is a mathematical group defined in the space of spherical surfaces equipped with the operation of rotation [12]. Since this is a group, it admits a definition of a convolution operation for spherical signals defined on the rotational group [13]. This gives rise to spherical convolutional filters, which are linear processing architectures that compute weighted, rotated linear combinations of the values of a spherical signal [14], [15].

Spherical convolutional filters exhibit the property of rotation equivariance, which means that they yield the same output irrespective of the rotation of the input spherical signal [16], [17]. This property is particularly useful when processing 3-D data where the information is contained in the relative location of the signal values, and not on their absolute position [18]–[20]. Thus, processing spherical signal by means of spherical convolutional filters, allows the resulting architecture to effectively exploit the data structure in extracting useful information irrespective of the specific rotation of the image.

Spherical convolutional filters are linear, and as such are restricted to capture only linear relationships between the input data and the relevant information. Spherical convolutional neural networks (Spherical CNNs) are nonlinear processing architectures that consists of a cascade of layers, each of which applies a spherical convolutional filter followed by a pointwise nonlinearity [16]. The inclusion of nonlinearities together with multiple layers dons Spherical CNNs with an enhanced representation power, capable of capturing nonlinear relationships, and exhibiting superior performance when processing spherical signals [16], [17], [21].

Considering the evident success of Spherical CNNs in processing 3-D surface data, in this paper, we focus on analyzing the properties that Spherical CNNs exhibit as they pertain to the rotational structure present in spherical signals. These properties offer an insight into the reasons behind the observed success of Spherical CNNs. We first show that they retain the rotation equivariance from spherical convolutional filters (Prop. 2). In the context of Spherical CNNs, rotation equivariance plays a key role in improving the learning process and the generalization capability by exploiting the data structure. More precisely, Spherical CNNs can learn how to process all rotated versions of an input image by just seeing one of them in the training set.

We further consider more general changes to the input images [22]. Specifically, if two images are close to being rotations of each other, we would like the processing architectures to yield similar outputs, since they likely capture the same information in their data structure. We thus define a notion of a rotation diffeomorphism (Def. 3), which is a local rotation of the image (i.e. a perturbation of the spherical space where each point in space may be rotated by a different angle). We prove that spherical convolutions with Lipschitz filters are stable to these perturbations (Thm. 1), and that this property is inherited by Spherical CNNs as well (Thm. 2). In short, we show that both spherical convolutional filters and Spherical CNNs exhibit the properties of rotation equivariance and stability to rotation diffeomorphisms, which allows them to exploit the

Supported by NSF CCF 1717120, ARO W911NF1710438, ARL DCIST CRA W911NF-17-2-0181, ISTC-WAS and Intel DevCloud. Z. Gao and A. Ribeiro are with the Dept. of Electrical and Systems Engineering, Univ. of Pennsylvania. F. Gama is with the Dept. of Electrical Engineering and Computer Sciences, Univ. of California, Berkeley. Email: {gaozhan, aribeiro}@seas.upenn.edu, fgama@berkeley.edu.

data structure to improve the learning process. Spherical CNNs tend to outperform spherical convolutional filters, due to their capability of representing nonlinear functions.

The value of processing architectures that are rotation equivariant and stable to rotation diffeomorphisms becomes apparent when considering a problem such as object identification [23]. For instance, a robot navigating a given space captures a LIDAR image of a chair (see Fig. 4) and wants to identify the object. Depending on how close the robot is to the chair, the resulting image may exhibit a prominent back rest (see Fig. 6b and Fig. 6c) or a larger seat (see Fig. 6d). However, these small changes in the image introduced by a different viewing angle (and modeled as a rotation diffeomorphism) should not affect the fact the observed object is still a chair. Thus, utilizing processing architectures that are stable to rotation diffeomorphisms is of paramount importance.

We begin the paper by introducing spherical convolutions built for spherical signals on the rotation group and defining spherical convolutional neural networks in Sec. II. We devote Sec. III to analyze structural properties of spherical convolutions. First, we show spherical convolutional filters are equivariant to rotations, implying that the same information can be extracted regardless of whether signals are rotated (Prop. 1). Then, we consider more general perturbations defined as rotation diffeomorphisms (Def. 3), and state that spherical convolutions with Lipschitz filters (Def. 4) are stable to such perturbations with a constant depending on the Lipschitz condition (Thm. 1). This indicates spherical convolutions yield similar outputs for signals that are perturbed by diffeomorphisms close to rotations. In Sec. IV, we carry over the rotation equivariance and diffeomorphism stability analysis from spherical convolutions to Spherical CNNs (Prop. 2 and Thm. 2). Sec. V provides numerical simulations to corroborate theoretical analysis on 3-D object classification problems and Sec. VI concludes the paper.

## II. SPHERICAL CONVOLUTIONAL NEURAL NETWORKS

Signals arising from 3-D data, e.g., LIDAR images, X-ray models, surface data, etc., can be better described as inscribed in a sphere contained in 3-D space [8], [9]. In Sec. II-A we introduce the mathematical description of these spherical signals, in Sec. II-C we discuss the spherical convolution as the fundamental linear operation between spherical signals, and in Sec. II-D we present the spherical convolutional neural network (Spherical CNN).

### A. Spherical signals

Let  $\mathbb{S}_2 \subset \mathbb{R}^3$  be the sphere space contained in  $\mathbb{R}^3$ . Given a coordinate system  $\mathcal{S}(x, y, z)$ , a point  $u = (x_u, y_u, z_u) \in \mathbb{S}_2$  can be described by two angular variables  $\theta_u$  and  $\phi_u$ , where  $\theta_u = \arctan(\sqrt{x_u^2 + y_u^2}/z_u) \in [0, \pi]$  is the polar angle from the  $z$ -direction and  $\phi_u = \arctan(x_u/y_u) \in [0, 2\pi)$  is the azimuth angle along the  $xy$ -plane. A point  $u \in \mathbb{S}_2$  is further parametrized by the distance  $d = \sqrt{x_u^2 + y_u^2 + z_u^2}$  from the origin but, without loss of generality, we set  $d = 1$ . See Fig. 1a

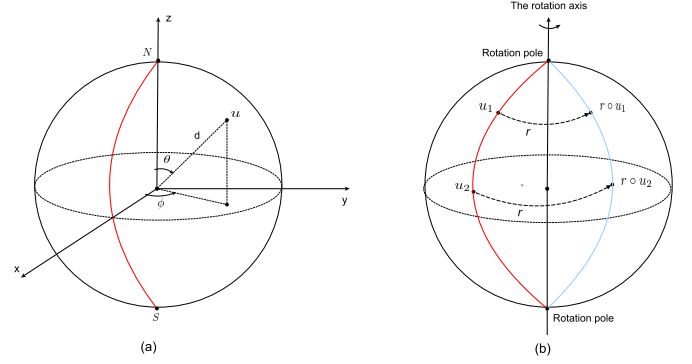


Figure 1. (a) The spherical coordinate system. A point on the sphere can be completely represented by the polar angle, the azimuth angle and the distance from the origin. (b) Azimuthal rotation on the sphere. The rotation displaces points on the sphere along the rotation axis, e.g., it displaces points on the red line to corresponding points on the blue line.

for details of the spherical coordinate system. In this context, a point  $u \in \mathbb{S}_2$  can be represented by the vector

$$u = (\theta_u, \phi_u) = [\sin(\theta_u) \cos(\phi_u), \sin(\theta_u) \sin(\phi_u), \cos(\theta_u)]. \quad (1)$$

For points whose polar angle are either  $\theta_u = 0$  or  $\theta_u = \pi$  the azimuth angle is assumed to be zero without loss of generality. These points are known as the north and south poles and denoted by  $N \in \mathbb{S}_2$  and  $S \in \mathbb{S}_2$ , respectively [cf. Fig. 1a].

A *spherical signal* is defined as the map  $x : \mathbb{S}_2 \rightarrow \mathbb{R}$  which assigns a scalar  $x(u) \in \mathbb{R}$  to each point  $u \in \mathbb{S}_2$  on the sphere. Equivalently, these signals can be described as mappings from the angular variables  $(\theta_u, \phi_u)$  to the real line  $\mathbb{R}$ , i.e.  $x(u) = x(\theta_u, \phi_u)$ . Spherical signals typically are used to describe data collected from 3-D objects. See Fig. 2 for an example on how to cast the surface of 3-D objects as spherical signals.

### B. The rotation operation

Rotations are elementary operations to which a spherical signal can be subject [10], [11]. A *rotation*  $r$  is completely characterized by the rotation point  $N^r \in \mathbb{S}_2$  and the rotation angle  $\beta^r \in [0, 2\pi)$ . In particular, it consists of displacing the points on the sphere by  $\beta^r$  degrees along the axis that passes through the origin and the point  $N^r$ ; thus, we refer to  $N^r$  as the rotation point or the rotation axis. To describe the rotation in the spherical coordinate system [cf. (1)], let  $r^\theta : \mathbb{S}_2 \rightarrow \mathbb{R}$  be the polar angle displacement and  $r^\phi : \mathbb{S}_2 \rightarrow \mathbb{R}$  be the azimuth angle displacement induced by the rotation. These two quantities parametrize the rotation operation  $r : \mathbb{S}_2 \rightarrow \mathbb{S}_2$  defined as

$$\begin{aligned} r \circ u &= r \circ (\theta_u, \phi_u) \\ &= [\sin(\theta_u + r^\theta(\theta_u, \phi_u)) \cos(\phi_u + r^\phi(\theta_u, \phi_u)), \\ &\quad \sin(\theta_u + r^\theta(\theta_u, \phi_u)) \sin(\phi_u + r^\phi(\theta_u, \phi_u)), \\ &\quad \cos(\theta_u + r^\theta(\theta_u, \phi_u))] \end{aligned} \quad (2)$$

where  $r^\theta$  and  $r^\phi$  are given by the Rodrigues' rotation formula [24]. The rotation operation takes a point  $u$  on the sphere  $\mathbb{S}_2$  and maps it into another point  $r \circ u$ , also in the sphere  $\mathbb{S}_2$ ,

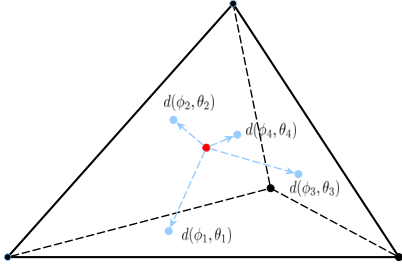


Figure 2. Spherical signal for the surface data of a tetrahedron. Consider a tetrahedron as the 3-D object, containing interior points from which the whole boundary is visible. Assume the object center as one of these interior points, from which we cast rays that intersect the object surface. Denote by  $d(\phi_u, \theta_u)$  the distance between the farthest intersection point and the center along the ray direction  $(\phi_u, \theta_u)$ , where  $\theta_u$  is the polar angle and  $\phi_u$  is the azimuthal angle. The surface data can then be represented as a spherical signal  $x(\phi_u, \theta_u) = d(\phi_u, \theta_u)$  with  $\phi_u \in [0, 2\pi)$  and  $\theta_u \in [0, \pi]$ , which maps the ray direction to the distance.

but where the polar angle has been displaced by  $r^\theta$  and the azimuthal angle by  $r^\phi$ . The rotation axis  $N^r$  intersects the spherical surface at two points, namely  $N^r \in \mathbb{S}_2$  which is referred to as the rotation north pole, and  $S^r \in \mathbb{S}_2$  which is referred to as the rotation south pole. These two points remain unchanged under the rotation operation. As an illustrative example, consider azimuthal rotations as shown in Fig. 1b, which are those where the rotation axis coincides with  $z$ -axis of the coordinate system  $\mathcal{S}(x, y, z)$ , i.e.  $N^r = N$  and  $S^r = S$ . Then,  $r^\theta(\theta_u, \phi_u) = 0$  and  $r^\phi(\theta_u, \phi_u) = \beta^r$  are constants for all  $(\theta_u, \phi_u) \in [0, \pi] \times [0, 2\pi)$ .

We can alternatively describe the rotation operation  $r \in \text{SO}(3)$  in terms of the  $ZYZ$  Euler parametrization as

$$r = r_{\phi_r \theta_r \rho_r} = r_{\phi_r}^z r_{\theta_r}^y r_{\rho_r}^z \quad (3)$$

where  $r_{\phi_r}^z$ ,  $r_{\theta_r}^y$  and  $r_{\rho_r}^z$  are the rotations along corresponding coordinate axis, each one with an angle of  $\phi_r \in [0, 2\pi)$ ,  $\theta_r \in [0, \pi]$  and  $\rho_r \in [0, 2\pi)$ , respectively. In other words, the Euler parametrization allows us to decompose any rotation  $r$ , determined by a rotation axis  $N^r$  and a rotation angle  $\beta^r$ , as three consecutive rotations, with rotation axes coinciding with each of the coordinate axes, and where each rotation angle is given by  $\phi_r$ ,  $\theta_r$  and  $\rho_r$ , respectively.

The set of rotation operations about the origin (2) defines a mathematical group under the operation of composition [25]. This group is usually called the *3-D rotation group* and is denoted as  $\text{SO}(3)$  [26]. This is a group in the sense that (i) composing two rotations  $r_1, r_2 \in \text{SO}(3)$  results in another rotation  $r_1 \circ r_2 \in \text{SO}(3)$ , (ii) rotations are associative ( $(r_1 \circ r_2) \circ r_3 = r_1 \circ (r_2 \circ r_3)$  for any  $r_1, r_2, r_3 \in \text{SO}(3)$ ), (iii) the rotation determined by  $r^\theta = r^\phi = 0$  is the identity rotation  $r_0 \in \text{SO}(3)$  such that  $r_0 \circ r = r$  for all  $r \in \text{SO}(3)$ , and (iv) for every rotation  $r \in \text{SO}(3)$  there exists another rotation  $r^{-1} \in \text{SO}(3)$ , such that  $r \circ r^{-1} = r_0$ .

### C. Spherical convolution

The sphere space  $\mathbb{S}_2$  is now equipped with a rotation operation that conforms a mathematical group. This allows us

to define a convolution operation for spherical signals. Given two signals  $x, h : \mathbb{S}_2 \rightarrow \mathbb{R}$  the spherical convolution  $*_{\text{SO}(3)}$  between them is defined as

$$y(u) = (h *_{\text{SO}(3)} x)(u) = \int_{\text{SO}(3)} h(r^{-1} \circ u) x(r) dr \quad (4)$$

where  $y(u)$  is the output spherical signal, and where we have used  $x(r)$  as a shorthand notation for  $x(r \circ u_0)$  with  $u_0 = (0, 0)$  the spherical point given by  $\theta_u = \phi_u = 0$ .

We can rewrite the convolution operation in terms of the Euler parametrization of a rotation [cf. (3)]. To do this, recall that the normalized Haar measure on the rotation group  $\text{SO}(3)$  can be written as [27]

$$dr = \frac{d\phi_r}{2\pi} \frac{\sin(\theta_r)}{2} \frac{d\theta_r}{2\pi} \frac{d\rho_r}{2\pi} \quad (5)$$

for normalized angles. We can then rewrite (4) as

$$\begin{aligned} y(u) &= (h *_{\text{SO}(3)} x)(u) \\ &= \frac{1}{8\pi^2} \int \left( h(r_{\phi_r \theta_r \rho_r}^{-1} \circ u) x(r_{\phi_r \theta_r \rho_r}) \right) \cdot \\ &\quad \sin(\theta_r) d\theta_r d\phi_r d\rho_r \end{aligned} \quad (6)$$

where  $r_{\phi_r \theta_r \rho_r}$  is the rotation parametrized by Euler angles  $\phi_r, \theta_r, \rho_r$  and  $r_{\phi_r \theta_r \rho_r}^{-1}$  is its inverse rotation. In the spherical coordinate system, by noting that  $r_{\phi_r \theta_r \rho_r} \circ u_0 = (\theta_r, \phi_r)$  and using Rodrigues' formula (2), we further get

$$\begin{aligned} y(\theta_u, \phi_u) &= (h *_{\text{SO}(3)} x)(\theta_u, \phi_u) \\ &= \frac{1}{8\pi^2} \int \left( h(\theta_u + r_{\phi_r \theta_r \rho_r}^{\theta-1}(\theta_u, \phi_u), \phi_u + r_{\phi_r \theta_r \rho_r}^{\phi-1}(\theta_u, \phi_u)) \cdot \right. \\ &\quad \left. x(\theta_r, \phi_r) \right) \cdot \sin(\theta_r) d\theta_r d\phi_r d\rho_r. \end{aligned} \quad (7)$$

where  $r_{\phi_r \theta_r \rho_r}^{\theta-1}$  and  $r_{\phi_r \theta_r \rho_r}^{\phi-1}$  are angle displacements induced by  $r_{\phi_r \theta_r \rho_r}^{-1}$ . We see that (7) is equivalent to (4) and (6), but described in terms of the polar angle  $\theta_u$  and azimuthal angle  $\phi_u$  on which we want to evaluate the output of the convolution. Thus, we moved from a description given entirely in the realm of the rotation group  $\text{SO}(3)$ , to a description given in term of the specific coordinates that describe a point in the spherical coordinate system (1). It is important to note that we have parametrized the rotation operations on polar and azimuth angles, namely  $r_{\phi_r \theta_r \rho_r}^{\theta}$  and  $r_{\phi_r \theta_r \rho_r}^{\phi}$ , in terms of the Euler angles. This allows us to carry out the integral in (7). Note that, since the integration is with respect to the element of the group  $r$  in (4), then it becomes an integral with respect to the parameters  $\theta_r, \phi_r, \rho_r$  that characterize this rotation element.

**Remark 1** (Group convolution). Convolution operations can be formally defined with respect to any group that is applicable to the space on which the convolving signals are defined. That is, let  $x, h : \mathbb{X} \rightarrow \mathbb{R}$  be two signals mapping some space  $\mathbb{X}$  into the real line, and let  $G = G(\mathbb{X}, \circ)$  be a group whose elements  $g \in G$  are defined over  $\mathbb{X}$ , whose binary operation we denote by  $\circ$  and where  $g^{-1} \in G$  is the inverse element. Then, the convolution operation  $*_G$  is generically defined as

$$(h *_G g)(u) = \int_{g \in G} h(g^{-1} \circ u) x(g \circ u_0) dg \quad (8)$$

for  $u, u_0 \in \mathbb{X}$ . The spherical convolution (4) is one instance of a group convolution, for  $G = \text{SO}(3)$ . Another example is the regular convolution, which is defined over the group of translations. We note that many of the results derived in this work are applicable to generic group convolutions as well, see [28] for details.

#### D. Spherical convolutional neural networks

Spherical convolutions are linear operations that exploit the rotational structure present in spherical signals. Thus, they can be used to regularize the linear transform in neural networks so that the resulting architecture leverages this structure when processing spherical signals from 3-D data.

A neural network is a nonlinear map that consists of a cascade of  $L$  layers, each of which applies a linear transform  $A_\ell$  followed by a pointwise nonlinearity  $\sigma_\ell$  as follows [29, Ch. 6]

$$x_\ell = \sigma_\ell \left[ A_\ell x_{\ell-1} \right], \quad \ell = 1, \dots, L \quad (9)$$

with  $x_0 = x$  being the input signal. The number of layers  $L$  as well as the specific form of the nonlinearity  $\sigma_\ell$  are typically a design choice, while the linear transforms  $\{A_\ell\}$  are *learned* by minimizing some objective function over a training set.

Neural networks in such a general form work well only for small input data size, otherwise the space of learnable linear transforms  $A_\ell$  becomes too large to be efficiently explored, and the resulting mapping rarely generalizes well [29, Ch. 9]. Successful neural network architectures like convolutional neural networks (CNNs) [30]–[32] or graph neural networks (GNNs) [33]–[35] regularize the space of linear transforms by imposing a structure on the operation  $A_\ell$ , typically exploiting what is known a priori about the input data (i.e., that CNNs take as input regular Euclidean data, or that GNNs take as input graph signals).

Working with spherical signals demands neural network architectures that are able to exploit the rotational structure. For this, we define the spherical convolutional neural network (Spherical CNN) where we regularize the linear transform  $A_\ell$  to be a spherical convolution (4), namely [16]

$$x_\ell = \sigma_\ell \left[ h_\ell *_{\text{SO}(3)} x_{\ell-1} \right], \quad \ell = 1, \dots, L \quad (10)$$

with  $x_0 = x$  the input signal. We see in (10) that the linear transform is now forced to be a spherical convolution. The learnable linear transforms are now the collection of filters  $\mathcal{H} = \{h_\ell\}_{\ell=1}^L$ , one per layer. We note that determining the description of these filters is also a design choice (for example, choosing a certain parametric family of filters and then learning the specific parameters from the training data).

The descriptive power of spherical signals can be increased by considering a multiple feature (multi-feature) signal mapping  $\mathbf{x} : \mathbb{S}_2 \rightarrow \mathbb{R}^F$ , where we map each point in the sphere to a  $F$ -dimensional vector instead of a scalar. Each entry of the vector is termed a *feature* and the multi-feature spherical signal can be thought of as a collection of  $F$  single-feature spherical signals  $x^f : \mathbb{S}_2 \rightarrow \mathbb{R}$ , i.e.  $\mathbf{x} = \{x^f\}_{f=1}^F$ . In this context, the convolution operation becomes a series of spherical convolutions where the input signal is processed

through a filter bank. More specifically, an output signal with  $G$  features  $\mathbf{y} : \mathbb{S}^2 \rightarrow \mathbb{R}^G$  can be obtained by, first, filtering the input  $\mathbf{x}$  through a bank of  $FG$  filters

$$y^{fg} = h^{fg} *_{\text{SO}(3)} x^f \quad (11)$$

for  $f = 1, \dots, F$ ,  $g = 1, \dots, G$ , and where each feature  $x^f$  is convolved with the filter  $h^{fg}$  to output the feature  $y^{fg}$ . Then, the output of each  $g$ th filter is aggregated for all input features

$$y^g = \sum_{f=1}^F y^{fg} \quad (12)$$

for each  $g = 1, \dots, G$ . Operations (11)–(12) together define the spherical convolution acting on multi-feature spherical signals, which is equivalent to filtering the  $F$  features of the input signal through a bank of  $FG$  filters and then aggregating the output of each  $g$ th filter across all  $F$  input features.

In what follows, to simplify notation, we will denote the spherical convolution as a filtering operation, i.e.  $y = H(x)$  where  $H$  can denote either a single spherical convolution with a single filter (4) or a multi-feature one with an appropriately-sized bank of filters, followed by aggregation (11)–(12). In any case, we also overload the symbol  $H$  to denote both the operation as well as the filter taps involved. With this notation in place, the Spherical CNN can be written as

$$x_\ell = \sigma_\ell \left[ H_\ell(x_{\ell-1}) \right], \quad \ell = 1, \dots, L \quad (13)$$

with  $x_0 = x$ . The output of the last layer is denoted as  $\Phi(x; \mathcal{H}) = x_L$  where  $\Phi : \mathbb{S}_2 \rightarrow \mathbb{S}_2$  represents the nonlinear mapping given by the Spherical CNN (13). The learnable parameters in the Spherical CNN consist of the filters  $\mathcal{H} = \{H_\ell\}_{\ell=1}^L$ . The design hyperparameters are the number of layers  $L$ , the specific nonlinearity  $\sigma_\ell$  and, if pertinent, the number of features  $F_\ell$  to output in each layer.

By making use of spherical convolutions (4) to regularize a neural network [cf. (9)], the resulting Spherical CNN (13) is designed to leverage the structure of 3-D data. Thus, we expect it to exhibit strong performance on tasks involving this kind of data (and, as a matter of fact, this is actually observed in practice [16]). In what follows, we demonstrate the properties of rotation equivariance and perturbation stability of Spherical CNNs. These two properties illustrate exactly how Spherical CNNs leverage the data structure, and help us understand the observed superior performance when processing 3-D data.

**Remark 2.** Oftentimes, convolutional neural networks include a multi-layer perceptron (concatenation of fully connected layers) after the last convolutional layer  $x_L$ , typically to adapt the dimension difference between the given data and the target representation. This last layer does not exploit the data structure. Also, to keep the dimensionality of  $x_\ell = \{x_\ell^f\}_{f=1}^{F_\ell}$  small, a pooling operation is included, by which each  $x_\ell^f$  is downsampled, while the number of features grows (i.e. the spatial dimension is traded for the feature dimension). In what follows, however, we focus only on the spherical convolutional layers and their interaction with the pointwise nonlinearities, and thus we consider the Spherical CNNs to be nonlinear maps between spherical signals.

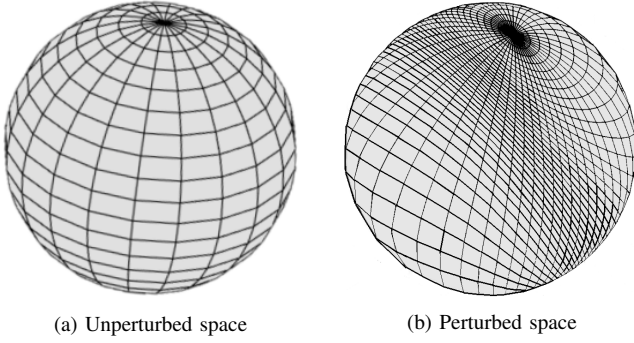


Figure 3. [22] Rotation diffeomorphism on the sphere [cf. Def 3]. (a) Unperturbed sphere. (b) Perturbed sphere after a rotation diffeomorphism.

### III. STRUCTURAL PROPERTIES OF SPHERICAL CONVOLUTIONS

Adopting the spherical convolution as the main operation to process spherical signals exploits the rotational structure of the data. For instance, when the input spherical signal is a rotated version of another one, then the output of the spherical convolution is a correspondingly rotated version, a property known as rotation equivariance (Sec. III-A). In terms of more general perturbations on the input spherical signal (Sec. III-B), spherical convolutions turn out to be stable when the changes are close to rotations (Sec. III-C).

#### A. Rotation equivariance

In most practical settings, the information contained in a spherical signal does not change under rotations. That is, the information that is relevant for the given application is present irrespective of the specific angle at which we are looking at the signal. For example, the surface and the shape of a 3-D object remains unchanged under rotation, and thus any shape analysis method should be equivariant to rotations [36], [37]. Therefore, it is of paramount importance that the processing tools that we choose are not affected by rotations as well.

Let  $r \in \text{SO}(3)$  be a rotation and  $x$  be a spherical signal. Define the rotated signal  $x_r$  as

$$x_r(u) = x(r \circ u) = x(\theta_u + r^\theta(\theta_u, \phi_u), \phi_u + r^\phi(\theta_u, \phi_u)) \quad (14)$$

for all  $u \in \mathbb{S}_2$ , and where the last equality responds to the rotation displacements following Rodrigues' formula [cf. (2)]. The rotation equivariance of spherical convolutions is formally stated next.

**Proposition 1.** *Let  $x$  be a spherical signal,  $H$  be a filter, and  $r \in \text{SO}(3)$  be a rotation. Denote by  $y = H(x)$  the output of the spherical convolution and  $y_r$  the rotated signal of  $y$  [cf. (14)]. Then, it holds that*

$$y_r = H(x_r). \quad (15)$$

*Proof.* See Appendix A.  $\square$

Proposition 1 states that applying a spherical convolutional filter  $H$  to a rotated version of the signal  $H(x_r)$  yields a rotated version of the output  $y_r$ , where  $y = H(x)$  is the

output of filtering the original signal. This indicates that the spherical convolution is capable of harnessing the same information irrespective of what rotated version of the signal is processed. Likewise, rotation equivariance serves to improve generalization and speed up training, since learning how to process one instance of the signal is equivalent to learning how to process all rotated versions of the same signal. This is analogous to the effect that translation equivariance has on CNNs [28] or permutation equivariance has on GNNs [38].

#### B. Signal dissimilarity modulo rotations

In general, we are more interested in how the processing architecture based on spherical convolutions fares when acting on two signals that are similar, but not quite the same. In a sense, we want the architecture to be able to tell apart signals when they are sufficiently different, and to give a similar output if the changes are due to noise or other unimportant cause [39]–[41]. The rotation equivariance property (Prop. 1) states that the same information is obtained when processing all rotated versions of a same signal. This suggests that to measure how (dis)similar two signals are, we need to abstract from the rotation or, in other words, we need to do it modulo rotations. Motivated by this consideration, we define the rotation distance as follows.

**Definition 1** (Rotation distance). *For two spherical signals  $x, \hat{x}$ , the rotation distance is defined as*

$$\|x - \hat{x}\|_{\text{SO}(3)} = \inf_{r \in \text{SO}(3)} \|x - \hat{x}_r\| \quad (16)$$

where  $\hat{x}_r(u) = \hat{x}(r \circ u)$  is the rotated spherical signal of  $\hat{x}$  and  $\|\cdot\|$  is the norm representation.

Any valid norm can be applied in the rotation distance (Def. 1). In the case of spherical signals, we adopt the following norm.

**Definition 2** (Normalized spherical norm). *For a spherical signal  $x : \mathbb{S}_2 \rightarrow \mathbb{R}$ , the normalized spherical norm is defined as*

$$\|x\|^2 = \frac{1}{2\pi^2} \int x(\theta_u, \phi_u)^2 d\theta_u d\phi_u. \quad (17)$$

where  $\theta_u \in [0, \pi]$  and  $\phi_u \in [0, 2\pi)$  describing the support  $u \in \mathbb{S}_2$  of the spherical signal  $x$  in the spherical coordinate system [cf. (1)]. For multi-feature spherical signals  $\mathbf{x} = \{x^f\}_{f=1}^F$ , we define  $\|\mathbf{x}\| = \sum_{f=1}^F \|x^f\|$ .

This is a proper norm in the sense that it is (i) absolutely scalable, (ii) positive definite, and (iii) satisfies the triangular inequality. Equipping the space of spherical signals with a norm allows us to define the following normed space

$$\mathbb{L}^2(\mathbb{S}_2) = \{\mathbf{x} : \mathbb{S}_2 \rightarrow \mathbb{R}^F : \|\mathbf{x}\| < \infty\} \quad (18)$$

Certainly, the  $\mathbb{L}^2(\mathbb{S}_2)$  space holds for single feature signals by setting  $F = 1$  in (18) and using the corresponding definition of spherical norm [cf. Def. 2]. In essence,  $\mathbb{L}^2(\mathbb{S}_2)$  is the space of finite-energy (single- or multi-feature) spherical signals.

Note that, if  $\hat{x}(u) = x(r \circ u) = x_r(u)$  is a rotated version of signal  $x$ , then  $\|x - \hat{x}\|_{\text{SO}(3)} = \|x - x_r\|_{\text{SO}(3)} = 0$ . Under the



dissimilarity measure given by the rotation distance (Def. 1), Prop. 1 can be reframed in terms of the following corollary.

**Corollary 1.** *Let  $x, \hat{x}$  be two spherical signals, and  $H$  be a filter. Then, it holds that*

$$\|x - \hat{x}\|_{\text{SO}(3)} = 0 \Rightarrow \|H(x) - H(\hat{x})\|_{\text{SO}(3)} = 0. \quad (19)$$

*Proof.* See Appendix B.  $\square$

Note that the rotation distance (16) is applied to spherical signals, but since the output of a filter is also a spherical signal, this same distance definition applies as well.

**Remark 3** (Group distance). Definition 1 can be extended to any group. In particular, let  $G = G(\mathbb{X}, \circ)$  be a group with elements  $g \in G$  defined over space  $\mathbb{X}$ , and  $x, \hat{x} : \mathbb{X} \rightarrow \mathbb{R}$  two group signals mapping  $\mathbb{X}$  to the real line  $\mathbb{R}$ . The group distance with respect to  $G$  is defined as

$$\|x - \hat{x}\|_G = \inf_{g \in G} \|x - \hat{x}_g\| \quad (20)$$

where  $\hat{x}_g(u) = \hat{x}(g \circ u)$  is the signal operated by  $g$  and any valid norm  $\|\cdot\|$  can be applied here. Certainly, the rotation group  $G = \text{SO}(3)$  is a particular case of this definition.

### C. Stability to Diffeomorphism Perturbations

In a general case, we are interested in perturbations of the signal that are small when measured with the rotation distance (Def. 1). In other words, we want the processing architecture to yield similar results when the signals are close to being rotated versions of each other.

Denote by  $r_u \in \text{SO}(3)$  the rotation operation that maps the origin point  $u_0 \in \mathbb{S}_2$  to the point  $u \in \mathbb{S}_2$  along the shortest arc, i.e.  $u = r_u \circ u_0$ . We are interested in perturbations  $\tau : \mathbb{S}_2 \rightarrow \mathbb{S}_2$  that can be described as local rotations, i.e. rotations whose characterization changes depending on the specific point  $u$  on which it is applied to. Let  $\tau \circ u$  be the resulting point after the perturbation  $\tau$  is applied. We can similarly obtain the point  $\tau \circ u = r_{\tau \circ u} \circ u_0$  by applying the rotation  $r_{\tau \circ u}$  to  $u_0$ . Combining the notions of  $r_u$  and  $r_{\tau \circ u}$  we can formally define an admissible perturbation as follows.

**Definition 3** (Admissible perturbations). *Let  $\tau : \mathbb{S}_2 \rightarrow \mathbb{S}_2$  be a diffeomorphism, i.e. a bijective differentiable function whose inverse  $\tau^{-1} : \mathbb{S}_2 \rightarrow \mathbb{S}_2$  is differentiable as well. This diffeomorphism can be used to define a local rotation  $\tau_u \in \text{SO}(3)$  as*

$$\tau_u = r_{\tau \circ u} \circ r_u^{-1}, \quad \forall u \in \mathbb{S}_2. \quad (21)$$

*The set of admissible perturbations are all the local rotations (21) that satisfy  $\|\tau\| < \infty$  and  $\|\nabla\tau\| < \infty$  for*

$$\|\tau\| := \max_{u \in \mathbb{S}_2} \left\{ \beta^{\tau_u} \right\}, \quad (22)$$

*where  $\beta^{\tau_u}$  is the rotation angle of the local rotation  $\tau_u$  [cf. (21)]; and for*

$$\|\nabla\tau\| = \max_{(\theta_u, \phi_u) \in [0, \pi] \times [0, 2\pi]} \left\{ \left| \frac{\partial \tau^\theta}{\partial \theta_u} \right|, \left| \frac{\partial \tau^\phi}{\partial \phi_u} \right| \right\}. \quad (23)$$

*where  $\tau^\theta$  and  $\tau^\phi$  are polar and azimuthal angle displacements induced by  $\tau$  such that  $\tau^\theta(\theta_u, \phi_u) = \tau_u^\theta(\theta_u, \phi_u)$  and  $\tau^\phi(\theta_u, \phi_u) = \tau_u^\phi(\theta_u, \phi_u)$  at each point  $u \in \mathbb{S}_2$ . The signal resulting from an admissible perturbation to the spherical structure of a given signal  $x$  is denoted as  $x_\tau$  such that*

$$x_\tau(u) = x(\tau \circ u), \quad \forall u \in \mathbb{S}_2. \quad (24)$$

*The diffeomorphism applied to the spherical signal is called a rotation diffeomorphism.*

The admissible perturbations (Def. 3) are, essentially, local rotations where rotation axes and rotation angles depend on specific points on the sphere. Under the rotation distance [cf. (16)], we have

$$\|x - x_\tau\|_{\text{SO}(3)} = \inf_{r \in \text{SO}(3)} \|x - x_{r \circ \tau}\| \quad (25)$$

Thus, if we want to measure the *size of the perturbation*, we need to do so modulo rotations. Define the closest rotation  $r^*$  to the diffeomorphism  $\tau$  as

$$r^* = \operatorname{argmin}_{r \in \text{SO}(3)} \max\{\|r^{-1} \circ \tau\|, \|\nabla(r^{-1} \circ \tau)\|\} \quad (26)$$

where  $r^{-1} \circ \tau$  is also a diffeomorphism but modulo rotation. The *perturbation size* modulo rotations is then measured by [cf. (22), (23)]

$$\|\tau\|_{\text{SO}(3)} = \|(r^*)^{-1} \circ \tau\|, \quad \|\nabla\tau\|_{\text{SO}(3)} = \|\nabla((r^*)^{-1} \circ \tau)\| \quad (27)$$

In this way, (27) links the perturbation size to the rotation distance (16), and determines how far from a rotation of  $x$  the actual perturbation  $x_\tau$  is [cf. (24)]. Note that if the admissible perturbation is a rotation, then  $\|\tau\|_{\text{SO}(3)} = \|\nabla\tau\|_{\text{SO}(3)} = 0$ . Likewise,  $\|\tau\|_{\text{SO}(3)} = \|\nabla\tau\|_{\text{SO}(3)} = 0$  implies that  $\tau$  is actually a rotation,  $\tau \in \text{SO}(3)$ . An example of a perturbation stemming from a rotation diffeomorphism is illustrated in Fig. 3.

We have now defined the admissible perturbations of the signal, as those that modify the underlying space  $\mathbb{S}_2$  by using local rotations, i.e. rotations whose size depends on the specific point in space [cf. Def. 3]. Next, we restrict our attention to the family of *Lipschitz filters*.

**Definition 4** (Lipschitz filters). *A filter  $h : \mathbb{S}_2 \rightarrow \mathbb{R}$  is a Lipschitz filter, if there exists a constant  $C_h$  such that*

$$|h(u)| \leq C_h, \quad \frac{|h(u_1) - h(u_2)|}{\|u_1 - u_2\|_2} \leq C_h \quad (28)$$

*for all  $u, u_1, u_2 \in \mathbb{S}_2$ , where  $\|\cdot\|_2$  is the Euclidean norm in  $\mathbb{R}^3$ . When we consider multi-feature signals, we say a filter  $H$  [cf. (11)-(12)] is Lipschitz if each of the FG single-feature filters  $h^{fg}$  satisfy (28).*

Now we can proceed to characterize the stability of the spherical convolution to admissible perturbations [cf. Def. 3] of the input.

**Theorem 1** (Stability of spherical filters). *Let  $x \in \mathbb{L}^2(\mathbb{S}_2)$  be a spherical signal, and  $H$  be a Lipschitz filter with constant*

$C_h$  [cf. Def 4]. Consider an admissible perturbation  $\tau$  [cf. Def 3] that satisfies

$$\|\tau\|_{\text{SO}(3)} \leq \epsilon, \quad \|\nabla\tau\|_{\text{SO}(3)} \leq \epsilon \leq \frac{1}{2}. \quad (29)$$

Then, for the rotation diffeomorphism  $x_\tau$  [cf. (24)] it holds that

$$\|H(x) - H(x_\tau)\|_{\text{SO}(3)} \leq 8C_h\epsilon\|x\| + \mathcal{O}(\epsilon^2) \quad (30)$$

*Proof.* See Appendix C.  $\square$

Theorem 1 establishes that spherical convolutions are stable to small perturbations in the domain (modulo rotations). More specifically, the difference in the output between filtering  $x$  or a perturbed version  $x_\tau$  of it, is bounded. In fact, it is bounded linearly by the size of the perturbation  $\epsilon$ , and the proportionality constant is given by  $8C_h$ . A careful design of the filter can reduce the constant  $C_h$  and thus lead to more stable filters. The constant term 8 depends on the domain, and can be improved by further restricting the class of filters. Theorem 1 reduces to Corollary 1 if the rotation diffeomorphism  $\tau$  reduces to a rotation  $r$ , i.e.  $\|\tau\|_{\text{SO}(3)} = \|\nabla\tau\|_{\text{SO}(3)} = 0$ .

In summary, Theorem 1 establishes that spherical convolutional filters are stable to small perturbations of the input (modulo rotations). More concretely, if we apply the filter to a perturbation of the signal (given by a rotation diffeomorphism), instead of applying it to the original signal, then the output changes proportionally to the size of the perturbation, with a proportionality constant given by the characteristics of the filter.

#### IV. STABILITY OF SPHERICAL CONVOLUTIONAL NEURAL NETWORKS

Spherical CNNs  $\Phi(x; \mathcal{H})$  [cf. (13)] are nonlinear processing architectures suited for processing 3-D data, and have the potential to learn nonlinear representations of the input. Spherical CNNs are capable of exploiting the data structure because they have the properties of rotation equivariance (Sec. IV-A) and stability to rotation diffeomorphisms (Sec. IV-B) which they inherit from the constitutive spherical convolutional filters.

##### A. Rotation equivariance of Spherical CNNs

The fact that the spherical convolution is rotation equivariant (Prop. 1) extends immediately to the Spherical CNN. This is because of the pointwise nature of the nonlinearities that do not affect the structure of the data.

**Proposition 2.** Let  $x$  be a spherical signal,  $\Phi(\cdot; \mathcal{H})$  be a Spherical CNN [cf. (13)], and  $r \in \text{SO}(3)$  be a rotation. Denote by  $x_r = x(r \circ u)$  the rotated signal of the input  $x$ . Then, it holds that

$$\|\Phi(x; \mathcal{H}) - \Phi(x_r; \mathcal{H})\|_{\text{SO}(3)} = 0. \quad (31)$$

*Proof.* See Appendix D.  $\square$

Proposition 2 demonstrates that the output of the Spherical CNN on the rotated spherical signal  $y = \Phi(x_r; \mathcal{H})$  is the corresponding rotated version of the original Spherical CNN output  $y_r = y(r \circ u)$ . This implies that Spherical CNNs are able

to capture the same information, irrespective of the specific rotation of the signal. Therefore, Prop. 2 suggests that the Spherical CNNs generalize well since they can learn how to process all rotated versions of a given image, by learning how to process one of them.

##### B. Stability to rotation diffeomorphisms of Spherical CNNs

The stability of the Spherical CNN to rotation diffeomorphisms (Def. 3) is inherited from the stability of spherical convolutions. The inclusion of nonlinearities in the processing pipeline affects the stability constant. In particular, we consider nonlinearities that are Lipschitz, as defined next.

**Definition 5** (Lipschitz nonlinearity). A nonlinearity  $\sigma : \mathbb{R} \rightarrow \mathbb{R}$  satisfying  $\sigma(0) = 0$  is Lipschitz if there exists a constant  $C_\sigma > 0$  such that

$$|\sigma(a) - \sigma(b)| \leq C_\sigma |a - b|, \quad \forall a, b \in \mathbb{R}. \quad (32)$$

When Spherical CNNs are built from Lipschitz filters (Def. 4) and use Lipschitz nonlinearities (Def. 5), then they inherit the stability to rotation diffeomorphisms (Def. 3) from spherical convolutions [cf. Theorem 1]

**Theorem 2.** Let  $x \in \mathbb{L}^2(\mathbb{S}_2)$  be a spherical signal, and  $\Phi(\cdot; \mathcal{H})$  be a Spherical CNN [cf. (13)] consisting of  $L$  layers, with  $F_\ell = F$  features per layer, built with Lipschitz filters with constant  $C_h$  [cf. Def 4] and Lipschitz nonlinearities with constant  $C_\sigma$  [cf. Def. 5]. Consider an admissible perturbation  $\tau$  [cf. Def 3] that satisfies

$$\|\tau\|_{\text{SO}(3)} \leq \epsilon, \quad \|\nabla\tau\|_{\text{SO}(3)} \leq \epsilon \leq \frac{1}{2}. \quad (33)$$

Then, for the rotation diffeomorphism  $x_\tau$  [cf. (24)] it holds that

$$\|\Phi(x; \mathcal{H}) - \Phi(x_\tau; \mathcal{H})\|_{\text{SO}(3)} \leq 8(C_\sigma C_h)^L F^{L-1} \epsilon \|x\| + \mathcal{O}(\epsilon^2) \quad (34)$$

*Proof.* See Appendix E.  $\square$

Theorem 2 determines that Spherical CNNs are stable to perturbations. More concretely, the difference between the output of a Spherical CNN applied to an input signal and to its perturbed version is bounded above proportionally to the size of the perturbation  $\epsilon$ . This means that if the signals are close to being rotations of each other, the output of the Spherical CNN will be close as well. The proportionality constant depends on the learned filters through the constant  $C_h$  and depends on the design choices through  $F$ ,  $L$  and  $C_\sigma$ . We see that the deeper the Spherical CNN is, the looser the bound is, mainly due to the propagation of the differences through the architecture. In any case, the difference in the output of the Spherical CNN is linear in the size of the perturbation, guaranteeing stability of the architecture.

In summary, Spherical CNNs inherit the rotation equivariance and stability to diffeomorphism property from spherical convolutional filters. These two properties explain how Spherical CNNs exploit the underlying spherical structure present in 3-Data.

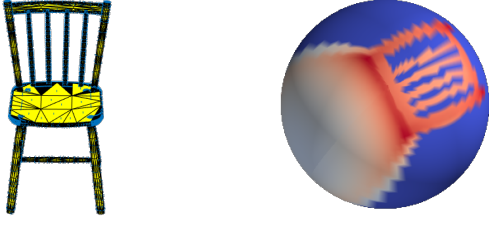


Figure 4. 3-D model (left) and spherical signal (right) of a chair.

**Remark 4.** Our results can be extended to any generic group  $G$  besides the rotation group  $SO(3)$ . I.e., the group operation equivariance and the group diffeomorphism (close to group operations) stability shall apply to the group convolution (8); hence, apply to the group convolutional neural network. Proofs of propositions and theorems can be carried out with similar processes, while the key step may be to find a suitable mathematical representation for the data structure of interest to perform theoretical analysis. For instance in the rotation group, the spherical coordinate system is utilized to describe 3-D data on the sphere, and the Euler parameterization is used to characterize the rotation group  $SO(3)$ .

## V. NUMERICAL EXPERIMENTS

We have proved that Spherical CNNs are rotation equivariant (Prop. 2) and that they are stable under rotation diffeomorphisms (Thm. 2). These properties illustrate how Spherical CNNs adequately exploit the data structure to improve their representation power and learning performance. As a matter of fact, they have already been shown successful in classification tasks [16]. Thus, in what follows, we focus solely on corroborating the theoretical properties by numerical simulations with controlled perturbations; for comparative performance with other methods, please refer to [16].

**Dataset and problem setting.** The shape classification problem of 3-D object is considered on the ModelNet40 dataset [23], i.e., given a spherical signal, the goal is to find out which class its represented object belongs to. There are 40 classes in the dataset, where we use 9683 samples for training and 29595 samples for testing. We parametrize the spherical signal in a  $64 \times 64$  resolution, see Fig. 4 for the 3-D model of a chair and its associated spherical signal as an example.

**Architectures and training.** We consider the Spherical CNN with 8 spherical convolutional layers, each of which contains 16, 16, 32, 32, 64, 64, 128 and 128 features respectively. The ReLU  $\sigma(\cdot) = \max\{\cdot, 0\}$  is used as the nonlinearity. For a readout layer, we apply a global weighted average pooling, obtaining a descriptor vector and the latter is projected into the number of object classes. We train the architecture for 50 epochs with the ADAM optimizer and a batch size of 16 samples. The learning rate is  $1 \cdot 10^{-3}$  and is divided by 5 on epochs 30 and 40, respectively. We start by evaluating the rotation equivariance, and then proceed to the diffeomorphism stability in the following.

Table I: Test classification accuracy of the Spherical CNN for the original dataset, 45 degree rotated dataset, 90 degree rotated dataset and 135 degree rotated dataset. Relative root mean square error (RMSE) of the Spherical CNN output features for 45 degree rotated dataset, 90 degree rotated dataset and 135 degree rotated dataset.

Rotation angle	Classification accuracy	Relative RMSE
0 degree	0.864	0
45 degree	0.864	$1.53 \cdot 10^{-3}$
90 degree	0.864	$1.45 \cdot 10^{-3}$
135 degree	0.864	$2.45 \cdot 10^{-3}$

Table II: Test classification accuracy of the Spherical CNN for Diffeomorphism 1-4. Relative root mean square error (RMSE) of the Spherical CNN output features for Diffeomorphism 1-4.

Diffeomorphism	Classification accuracy	Relative RMSE
Type 1	0.863	0.0614
Type 2	0.856	0.0801
Type 3	0.858	0.0715
Type 4	0.828	0.1152

**Rotation equivariance.** Given a trained Spherical CNN, we consider the test data rotated by 45 degree, 90 degree and 135 degree, respectively. Fig. 5 displays the resulting spherical signals under three rotations. We compute the output of the Spherical CNN on the original and rotated test sets. We show in Table I the resulting classification accuracy, and note that it remains the same, evidence that the Spherical CNN is rotation equivariant. We also show the relative root mean squared error (RMSE) between the features at the output of the Spherical CNN when applied to the original signal and the rotated signal. We see that it is virtually the same output, as expected.

**Diffeomorphism types.** We now test the change in the output of a Spherical CNN when the input signals are subject to four different types of diffeomorphisms. Namely, we carry out local rotations along the latitude, indicating different orders of perturbation severity. For type 1, we rotate every other sampled point at each latitude with a random degree drawn from the interval  $[-3, 3]$ , where we assume the clockwise direction as the positive direction. Type 2 rotates every other sampled point with a random degree drawn from the interval  $[-6, 6]$ . Type 3 considers rotations of each sampled point with a random degree drawn from the interval  $[-3, 3]$ . Finally, type 4 perturbs blocks of 3 samples at each latitude separately, rotating the second point to the third point and interpolating the values of the remaining sampled points, where the maximal degree change is then approximately 6 degrees. Fig. 6 shows examples of perturbed spherical signals that are associated to the aforementioned four types of rotation diffeomorphisms.

**Stability to perturbations.** Table II shows the classification accuracy of the trained Spherical CNN when assuming that all signals in the test set have been perturbed following each of the aforementioned diffeomorphism types. In general, the Spherical CNN exhibits strong robustness to the rotation diffeomorphism in all four cases, as was expected from Theorem 2. We observe that type 1 has little effect on the classification accuracy, while types 2 and 3 slightly decrease the accuracy, likely due to the increase of the maximal degree



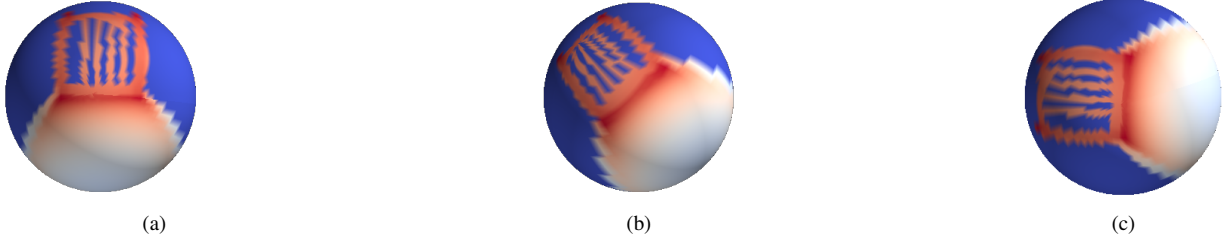


Figure 5. Rotations on the spherical signal. (a) 45 degree rotation. (b) 90 degree rotation. (c) 135 degree rotation.

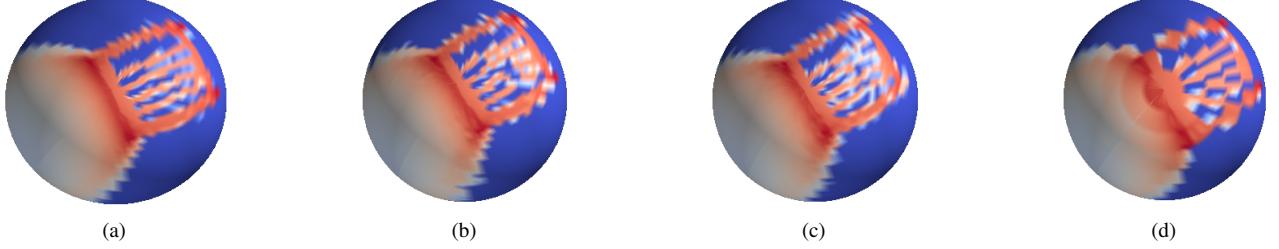


Figure 6. Rotation diffeomorphism on the spherical signal. (a) Type 1. (b) Type 2. (c) Type 3. (d) Type 4.

change and the number of perturbed sampled points. Finally, we note that type 4 is most severe as observed from Fig. 6d. However, the Spherical CNN only suffers from 0.036 accuracy loss, indicating the stability of the Spherical CNN to the rotation diffeomorphism. Similarly, Table II shows the relative root mean square error of the output features of the final spherical convolution layer under above rotation diffeomorphisms. The relative RMSE maintain low values in all cases, which indicates the Spherical CNN diffeomorphism stability. A higher classification accuracy typically corresponds to a lower relative RMSE.

## VI. CONCLUSIONS

Spherical convolutional neural networks comprises a cascade of layers, each of which applies a bank of spherical convolutions followed by a pointwise nonlinearity. As such, they inherit from spherical convolutions, the properties of rotation equivariance and stability to rotation diffeomorphisms (provided that the filters involved are Lipschitz). The former states that Spherical CNNs are capable of learning the output of all rotated versions of a signal by learning from one such instance, while the latter establishes that as long as two signals are similar, the output will be similar. These two properties illustrate the ways in which Spherical CNNs are capable of exploiting the rotational structure in 3-D data, and thus generalize well to unseen test samples. These theoretical results were corroborated through a controller numerical experiment.

### APPENDIX A

#### ROTATION EQUIVARIANCE OF SPHERICAL CONVOLUTIONS

*Proof of Proposition 1.* The spherical convolution between the rotated input  $x_r$  and the filter  $H$  is

$$\begin{aligned} H(x_r)(u) &= \int_{\text{SO}(3)} h(\hat{r}^{-1} \circ u) x(r \circ \hat{r}) d\hat{r} \\ &= \int_{\text{SO}(3)} h((r \circ \hat{r})^{-1} \circ (r \circ u)) x(r \circ \hat{r}) d\hat{r}, \end{aligned} \quad (35)$$

where the associativity of rotation operations is used. By defining  $r' = r \circ \hat{r}$ , we get

$$\begin{aligned} H(x_r)(u) &= \int_{\text{SO}(3)} h(r'^{-1} \circ (r \circ u)) x(r') dr' \\ &= h *_{\text{SO}(3)} x(r \circ u) = H(x)(r \circ u). \end{aligned} \quad (36)$$

Note that (36) holds for any point  $u \in \text{SO}(3)$ , and thus it holds for the spherical signal  $x$ . By letting  $y = H(x)$ , we complete the proof

$$H(x_r) = y_r. \quad (37)$$

□

### APPENDIX B

#### ROTATION EQUIVARIANCE UNDER ROTATION DISTANCE

*Proof of Corollary 1.* From  $\|x - \hat{x}\|_{\text{SO}(3)} = 0$ , we know that there exists a rotation  $r$  such that  $\hat{x} = x_r$  is a rotated signal of  $x$ . Denote by  $y = H(x)$  the spherical convolutional output and we have  $H(x_r) = y_r$  from Proposition 1. Under the rotation distance, we get

$$\begin{aligned} \|H(x) - H(\hat{x})\|_{\text{SO}(3)} &= \inf_{\tilde{r} \in \text{SO}(3)} \|y - y_{\tilde{r} \circ r}\| \\ &\leq \|y - y_{r^{-1} \circ r}\| = 0. \end{aligned} \quad (38)$$

Since  $\|H(x) - H(\hat{x})\|_{\text{SO}(3)} \geq 0$  by default, we have  $\|H(x) - H(\hat{x})\|_{\text{SO}(3)} = 0$  completing the proof. □

### APPENDIX C

#### STABILITY OF SPHERICAL CONVOLUTIONS

*Proof of Theorem 1.* Under the rotation distance, the output difference of the spherical convolution induced by the rotation diffeomorphism  $\tau$  is

$$\begin{aligned} \|H(x_\tau) - H(x)\|_{\text{SO}(3)} &= \inf_{r \in \text{SO}(3)} \|H(x_\tau) - r \circ H(x)\| \\ &= \inf_{r \in \text{SO}(3)} \|H(x_\tau) - H(x_r)\| \leq \|H(x_\tau) - H(x_{r^*})\| \end{aligned} \quad (39)$$

where the rotation equivariance of the spherical convolution is used and  $r^* \in \text{SO}(3)$  is the closest rotation to  $\tau$  defined as  $r^* = \text{argmin}_{r \in \text{SO}(3)} \max\{\|r^{-1} \circ \tau\|, \|\nabla(r^{-1} \circ \tau)\|\}$  [cf. (26)]. Since the normalized spherical norm is rotation invariant, i.e.,  $\|x_r\| = \|x\|$  for all  $r \in \text{SO}(3)$ , we have

$$\begin{aligned} \|H(x_\tau) - H(x_{r^*})\| &= \|(H(x_\tau))_{r^*} - (H(x_{r^*}))_{r^*}\| \quad (40) \\ &= \|H(x_{r^*} \circ \tau) - H(x_{r^*} \circ \tau^*)\| = \|H(x_{r^*} \circ \tau) - H(x)\| \end{aligned}$$

where  $(H(x))_{r^*}$  is the rotated signal of  $H(x)$  by the rotation  $r^*$ . Let  $\tau^* = r^* \circ \tau$  is the diffeomorphism module rotations. Let also  $Hx = H(x)$  and  $P_\tau^* x = x_{\tau^*}$  in operator notation. By substituting (40) into (39), we get

$$\|H(x_\tau) - H(x)\|_{\text{SO}(3)} \leq \|HP_\tau^* x - Hx\| = \|(HP_\tau^* - H)x\|.$$

We consider the operator  $HP_\tau^* - H$  and factorize it as

$$HP_\tau^* - H = (H - HP_\tau^{*-1}) P_\tau^*. \quad (41)$$

where  $P_\tau^{*-1}$  is the inverse operator of  $P_\tau^*$ , which exists since  $\tau^*$  is a diffeomorphism. The triangle inequality allows yields

$$\|HP_\tau^* - H\| = \|(H - HP_\tau^{*-1}) P_\tau^*\| \leq \|P_\tau^*\| \|H - HP_\tau^{*-1}\|. \quad (42)$$

Let us analyze two terms in the bound of (42) separately.

For the first term  $\|P_\tau^*\|$ , a known procedure to bound the norm of an operator  $P_\tau^*$  is to find an upper bound for the norm of  $\|P_\tau^* x\|$  as  $\|P_\tau^* x\| \leq A\|x\|$  for any spherical signal  $x$ . In this instance,  $A$  is the upper bound for the norm of  $\|P_\tau^*\|$ . Following this intuition, we have

$$\begin{aligned} \|P_\tau^* x\|^2 &= \frac{1}{2\pi^2} \int P_\tau^* x(\theta_u, \phi_u)^2 d\theta_u d\phi_u \quad (43) \\ &= \frac{1}{2\pi^2} \int x(\theta_u + \tau^{*\theta}(\phi_u, \theta_u), \phi_u + \tau^{*\phi}(\phi_u, \theta_u))^2 d\theta_u d\phi_u \end{aligned}$$

where  $\tau^{*\theta}$  and  $\tau^{*\phi}$  are polar and azimuth angle displacements induced by  $\tau^*$ . Denote by  $\hat{\theta}_u = \theta_u + \tau^{*\theta}(\phi_u, \theta_u)$  and  $\hat{\phi}_u = \phi_u + \tau^{*\phi}(\phi_u, \theta_u)$  the variable substitution. Then, we have to write (43) as an integration with respect to  $d\hat{\theta}_u d\hat{\phi}_u$ , instead of  $d\theta_u d\phi_u$ . To this end, see that

$$\begin{aligned} d\hat{\theta}_u d\hat{\phi}_u &= \left(1 + \frac{\partial \tau^{*\theta}}{\partial \theta_u}(\theta_u, \phi_u)\right) \left(1 + \frac{\partial \tau^{*\phi}}{\partial \phi_u}(\theta_u, \phi_u)\right) d\theta_u d\phi_u \\ &\geq (1 - \|\nabla \tau\|_{\text{SO}(3)})^2 d\theta_u d\phi_u, \quad (44) \end{aligned}$$

where the last inequality is due to the definition of  $\|\nabla \tau\|_{\text{SO}(3)}$  [cf. (27)]. From (44) we get  $d\theta_u d\phi_u \leq (1 - \|\nabla \tau\|_{\text{SO}(3)})^{-2} d\hat{\theta}_u d\hat{\phi}_u$ , and substituting it into (43), yields

$$\begin{aligned} \|P_\tau^* x\|^2 &\leq \frac{1}{2\pi^2} \int x(\hat{\theta}_u, \hat{\phi}_u)^2 (1 - \|\nabla \tau\|_{\text{SO}(3)})^{-2} d\hat{\theta}_u d\hat{\phi}_u \\ &= (1 - \|\nabla \tau\|_{\text{SO}(3)})^{-2} \|x\|^2 \leq 4\|x\|^2, \quad (45) \end{aligned}$$

where the condition  $\|\nabla \tau\|_{\text{SO}(3)} \leq 1/2$  is used in the last inequality. Thus, we have  $\|P_\tau^*\| \leq 2$ .

For the second term  $\|H - HP_\tau^{*-1}\|$ , let  $P_\tau^{*-1} x(u) = x(\xi \circ u)$  where  $\xi$  is the inverse operation of  $\tau^*$ , and we have

$$Hx(u) = \int_{\text{SO}(3)} h(r^{-1} \circ u) x(r) dr, \quad (46)$$

$$HP_\tau^{*-1} x(u) = \int_{\text{SO}(3)} h(r^{-1} \circ u) x(\xi \circ (r \circ u_0)) dr. \quad (47)$$

where  $u_0 = (0, 0)$  is the original point given by  $\theta_u = \phi_u = 0$ . For (46), we can rewrite it by parametrizing rotations with the Euler angles [cf. (7)]

$$Hx(u) = \frac{1}{8\pi^2} \int h(r_{\phi_r \theta_r \rho_r}^{-1} \circ u) x(\theta_r, \phi_r) \sin(\theta_r) d\theta_r d\phi_r d\rho_r$$

where  $r_{\phi_r \theta_r \rho_r}$  is the rotation characterized by the Euler angles  $(\phi_r, \theta_r, \rho_r)$ , and  $r_{\phi_r \theta_r \rho_r}^{-1}$  is its inverse rotation. For (47), by letting  $\xi_r = \xi \circ r$ , we have

$$HP_\tau^{*-1} x(u) = \int_{\text{SO}(3)} h(r^{-1} \circ u) x(\xi_r \circ u_0) dr. \quad (48)$$

Let  $(\theta_r, \phi_r)$  be polar and azimuth angle displacements of  $\xi_r$  at  $u_0$ , i.e.,  $\xi_r \circ u_0 = (\theta_r, \phi_r)$ . Since  $\xi^{-1} = \tau^*$ , we get

$$\begin{aligned} r \circ u_0 &= \xi^{-1} \circ (\xi_r \circ u_0) = \tau^* \circ (\xi_r \circ u_0) \quad (49) \\ &= (\theta_r + \tau^{*\theta}(\theta_r, \phi_r), \phi_r + \tau^{*\phi}(\theta_r, \phi_r)). \end{aligned}$$

We can then similarly rewrite (48) by parametrizing rotations with the Euler angles

$$\begin{aligned} HP_\tau^{*-1} x(u) &= \frac{1}{8\pi^2} \int x(\theta_r, \phi_r) \alpha(\theta_r, \phi_r) \sin(\theta_r + \tau^{*\theta}(\theta_r, \phi_r)) \cdot \\ &\quad h((r_{\tau^* \circ (\theta_r, \phi_r)} \circ r_{\rho_r}^Z)^{-1} \circ u) d\theta_r d\phi_r d\rho_r \quad (50) \end{aligned}$$

with

$$\alpha(\theta_r, \phi_r) = \left(1 + \frac{\partial \tau^{*\theta}(\theta_r, \phi_r)}{\partial \theta_r}\right) \left(1 + \frac{\partial \tau^{*\phi}(\theta_r, \phi_r)}{\partial \phi_r}\right) \quad (51)$$

where  $r_{\tau^* \circ (\theta_r, \phi_r)}$  is the rotation that rotates the original point  $(0, 0)$  to the point  $\tau^* \circ (\theta_r, \phi_r)$  along the shortest arc, i.e.,  $\tau^* \circ (\theta_r, \phi_r) = r_{\tau^* \circ (\theta_r, \phi_r)} \circ (0, 0)$ ,  $r_{\rho_r}^Z$  is the rotation along  $z$ -axis by  $\rho_r$  angles, and  $(r_{\tau^* \circ (\theta_r, \phi_r)} \circ r_{\rho_r}^Z)^{-1} = r_{\rho_r}^{Z^{-1}} \circ \tau_{\tau^* \circ (\theta_r, \phi_r)}^{*-1}$  is its inverse rotation.

By substituting (48) and (50) into the operator  $Hx - HP_\tau^{*-1} x$ , we get

$$\begin{aligned} Hx(u) - HP_\tau^{*-1} x(u) &= \frac{1}{8\pi^2} \int x(\theta_r, \phi_r) [h(r_{\phi_r \theta_r \rho_r}^{-1} \circ u) \sin(\theta_r) \\ &\quad - h(r_{\rho_r}^{Z^{-1}} \circ r_{\tau^* \circ (\theta_r, \phi_r)}^{-1} \circ u) \alpha(\theta_r, \phi_r) \sin(\theta_r + \tau^{*\theta}(\theta_r, \phi_r))] d\theta_r d\phi_r d\rho_r \\ &= \frac{1}{8\pi^2} \int k(\theta_r, \phi_r, \rho_r, \theta_u, \phi_u) x(\theta_r, \phi_r) d\theta_r d\phi_r d\rho_r \quad (52) \end{aligned}$$

where  $(\theta_u, \phi_u)$  is the equivalent description of  $u$  in the spherical coordinate system and  $k(\theta_r, \phi_r, \rho_r, \theta_u, \phi_u)$  can be considered as the kernel of the operator  $H - HP_\tau^{*-1}$ . Recall the Schur's Lemma [42]. For the operator  $K$  with kernel  $k(\theta_r, \phi_r, \rho_r, \theta_u, \phi_u)$ , if

$$\frac{1}{8\pi^2} \int |k(\theta_r, \phi_r, \rho_r, \theta_u, \phi_u)| d\theta_r d\phi_r d\rho_r \leq A, \quad (53)$$

$$\frac{1}{2\pi^2} \int |k(\theta_r, \phi_r, \rho_r, \theta_u, \phi_u)| d\theta_u d\phi_u \leq A, \quad (54)$$

we have  $\|K\| \leq A$ . We proceed by using the Schur's Lemma.

We divide  $k(\theta_r, \phi_r, \rho_r, \theta_u, \phi_u)$  into two sub-operators as

$$\begin{aligned} k(\theta_r, \phi_r, \rho_r, \theta_u, \phi_u) &= k_1(\theta_r, \phi_r, \rho_r, \theta_u, \phi_u) + k_2(\theta_r, \phi_r, \rho_r, \theta_u, \phi_u) \quad (55) \\ &= (1 - \alpha(\theta_r, \phi_r)) h(r_{\phi_r \theta_r \rho_r}^{-1} \circ u) \sin(\theta_r) \\ &\quad + \alpha(\theta_r, \phi_r) [h(r_{\phi_r \theta_r \rho_r}^{-1} \circ u) \sin(\theta_r) \\ &\quad - h(r_{\rho_r}^{Z^{-1}} \circ r_{\tau^* \circ (\theta_r, \phi_r)}^{-1} \circ u) \sin(\theta_r + \tau^{*\theta}(\theta_r, \phi_r))], \end{aligned}$$

and analyze these two sub-operators separately.

For the first sub-operator  $k_1(\theta_r, \phi_r, \rho_r, \theta_u, \phi_u)$ , since  $|\partial \tau^{\ast\theta}(\theta_r, \phi_r)/\partial \theta_r| \leq \|\nabla \tau\|_{\text{SO}(3)}$  and  $|\partial \tau^{\ast\phi}(\theta_r, \phi_r)/\partial \phi_r| \leq \|\nabla \tau\|_{\text{SO}(3)}$  [cf. (27)], we have

$$|1 - \alpha(\theta_r, \phi_r)| \leq (2 + \|\nabla \tau\|_{\text{SO}(3)}) \|\nabla \tau\|_{\text{SO}(3)}. \quad (56)$$

By substituting (56) into  $k_1(\theta_r, \phi_r, \rho_r, \theta_u, \phi_u)$ , we obtain

$$|k_1(\theta_r, \phi_r, \rho_r, \theta_u, \phi_u)| \leq |1 - \alpha(\theta_r, \phi_r)| |h(r_{\phi_r, \theta_r, \rho_r}^{-1} \circ u)| \leq C_h (2 + \|\nabla \tau\|_{\text{SO}(3)}) \|\nabla \tau\|_{\text{SO}(3)} \leq 2C_h \epsilon + \mathcal{O}(\epsilon^2) \quad (57)$$

where the last inequality uses the conditions that  $h$  is a Lipschitz filter with respect to  $C_h$  and  $\|\nabla \tau\|_{\text{SO}(3)} \leq \epsilon$ .

For the second sub-operator  $k_2(\theta_r, \phi_r, \rho_r, \theta_u, \phi_u)$ , similarly as (56), we have

$$|\alpha(\theta_r, \phi_r)| \leq 1 + 2\|\nabla \tau\|_{\text{SO}(3)} + \|\nabla \tau\|_{\text{SO}(3)}^2. \quad (58)$$

Then consider the reduction term  $h(r_{\phi_r, \theta_r, \rho_r}^{-1} \circ u) \sin(\theta_r) - h(r_{\rho_r}^{z-1} \circ r_{\tau^{\ast\theta}(\theta_r, \phi_r)}^{-1} \circ u) \sin(\theta_r + \tau^{\ast\theta}(\theta_r, \phi_r))$ , which can be divided into two sub-terms as

$$\begin{aligned} & \sin(\theta_r) [h(r_{\phi_r, \theta_r, \rho_r}^{-1} \circ u) - h(r_{\rho_r}^{z-1} \circ r_{\tau^{\ast\theta}(\theta_r, \phi_r)}^{-1} \circ u)] \\ & + h(r_{\rho_r}^{z-1} \circ r_{\tau^{\ast\theta}(\theta_r, \phi_r)}^{-1} \circ u) [\sin(\theta_r) - \sin(\theta_r + \tau^{\ast\theta}(\theta_r, \phi_r))] \end{aligned} \quad (59)$$

For the first term in (59), it is determined by two points  $r_{\phi_r, \theta_r, \rho_r}^{-1} \circ u$  and  $r_{\rho_r}^{z-1} \circ r_{\tau^{\ast\theta}(\theta_r, \phi_r)}^{-1} \circ u$ . With the Euler angle parametrization [cf. (3)], we have

$$r_{\phi_r, \theta_r, \rho_r}^{-1} \circ u = r_{\rho_r}^{z-1} \circ r_{(\theta_r, \phi_r)}^{-1} \circ u \quad (60)$$

where  $r_{(\theta_r, \phi_r)}$  is the rotation that rotates  $(0, 0)$  to  $(\theta_r, \phi_r)$  along the shortest arc. First consider two points  $r_{\tau^{\ast\theta}(\theta_r, \phi_r)}^{-1} \circ u$  and  $r_{(\theta_r, \phi_r)}^{-1} \circ u$ . Due to the symmetry of the sphere, we can alternatively consider corresponding two points  $r_{\tau^{\ast\theta}(\theta_r, \phi_r)} \circ u$  and  $r_{(\theta_r, \phi_r)} \circ u$  such that

$$\begin{aligned} r_{\tau^{\ast\theta}(\theta_r, \phi_r)} \circ u &= r_{\tau^{\ast\theta}(\theta_r, \phi_r)} \circ r_{(\theta_r, \phi_r)}^{-1} \circ (r_{(\theta_r, \phi_r)} \circ u) \\ &= \tau_{(\theta_r, \phi_r)}^{\ast} \circ (r_{(\theta_r, \phi_r)} \circ u) \end{aligned} \quad (61)$$

where  $\tau_{(\theta_r, \phi_r)}^{\ast}$  is the local rotation of  $\tau^{\ast}$  at the point  $(\theta_r, \phi_r)$  [cf. (21)], whose rotation angle is bounded by  $\|\tau\|_{\text{SO}(3)}$  [cf. (27)]. The shortest arc connecting these two points on the sphere is then bounded by

$$\text{arc}(r_{(\theta_r, \phi_r)} \circ u, r_{\tau^{\ast\theta}(\theta_r, \phi_r)} \circ u) \leq \|\tau\|_{\text{SO}(3)}, \quad \forall u \in \mathbb{S}_2 \quad (62)$$

since points are defined on the unit sphere. Thus, due to the symmetry of the sphere, we have

$$\text{arc}(r_{(\theta_r, \phi_r)}^{-1} \circ u, r_{\tau^{\ast\theta}(\theta_r, \phi_r)}^{-1} \circ u) \leq \|\tau\|_{\text{SO}(3)}, \quad \forall u \in \mathbb{S}_2. \quad (63)$$

Since  $r_{\rho_r}^{z-1}$  is the rotation along  $z$ -axis that does not change the distance between two points on the sphere, we get

$$\text{arc}(r_{\rho_r}^{z-1} \circ r_{(\theta_r, \phi_r)}^{-1} \circ u, r_{\rho_r}^{z-1} \circ r_{\tau^{\ast\theta}(\theta_r, \phi_r)}^{-1} \circ u) \leq \|\tau\|_{\text{SO}(3)} \quad (64)$$

for all  $u \in \mathbb{S}_2$ . With the Lipschitz property of filter  $h$ , we get

$$\begin{aligned} & |h(r_{(\theta_r, \phi_r)}^{-1} \circ u) - h(r_{\tau^{\ast\theta}(\theta_r, \phi_r)}^{-1} \circ u)| \\ & \leq C_h \|r_{\rho_r}^{z-1} \circ r_{(\theta_r, \phi_r)}^{-1} \circ u - r_{\rho_r}^{z-1} \circ r_{\tau^{\ast\theta}(\theta_r, \phi_r)}^{-1} \circ u\|_2 \\ & \leq C_h \text{arc}(r_{\rho_r}^{z-1} \circ r_{(\theta_r, \phi_r)}^{-1} \circ u, r_{\rho_r}^{z-1} \circ r_{\tau^{\ast\theta}(\theta_r, \phi_r)}^{-1} \circ u) \leq C_h \|\tau\|_{\text{SO}(3)} \end{aligned} \quad (65)$$

where  $|\sin(\theta_r)| \leq 1$  is used.

For the second term in (59), by using the truncated Taylor Expansion, we represent  $\sin(\theta_r + \tau^{\ast\theta}(\theta_r, \phi_r))$  as

$$\begin{aligned} & \sin(\theta_r + \tau^{\ast\theta}(\theta_r, \phi_r)) \\ & = \sin(\theta_r) + \cos(\theta_r + t\tau^{\ast\theta}(\theta_r, \phi_r)) \tau^{\ast\theta}(\theta_r, \phi_r) \end{aligned} \quad (66)$$

with some  $t \in (0, 1)$ . Now denote by  $u_1 = (\theta_r, \phi_r)$  and  $u_2 = \tau^{\ast} \circ u_1 = u(\theta_r + \tau^{\ast\theta}(\theta_r, \phi_r), \phi_r + \tau^{\ast\phi}(\theta_r, \phi_r))$  two points on the sphere, and consider the triangle  $\Delta u_1 u_0 u_2$  with  $u_0 = (0, 0)$ . Since the difference between two sides of the triangle is less than the third side, we have

$$|u_0 u_1 - u_0 u_2| \leq u_1 u_2 \quad (67)$$

Therefore, we get

$$|\text{arc}(u_0, u_1) - \text{arc}(u_0, u_2)| \leq \text{arc}(u_1, u_2). \quad (68)$$

Also since  $u_2 = \tau^{\ast} \circ u_1 = \tau_{u_1}^{\ast} \circ u_1$  where  $\tau_{u_1}^{\ast}$  is the local rotation of  $\tau^{\ast}$  at the point  $u_1$  and  $\text{arc}(u_1, u_2)$  is the shortest distance between  $u_1$  and  $u_2$ , we have  $\text{arc}(u_1, u_2) \leq \|\tau\|_{\text{SO}(3)}$ . By using this result in (68), we have

$$|\theta_r + \tau^{\ast\theta}(\theta_r, \phi_r) - \theta_r| = |\tau^{\ast\theta}(\theta_r, \phi_r)| \leq \|\tau\|_{\text{SO}(3)}. \quad (69)$$

where  $\text{arc}(u_0, u_1) = \theta_r$  and  $\text{arc}(u_0, u_2) = \theta_r + \tau^{\ast\theta}(\theta_r, \phi_r)$  hold due to the unit sphere. By substituting (69) into (66) and the latter into the second term in (59), we get

$$\begin{aligned} & |h(r_{\rho_r}^{z-1} \circ r_{\tau^{\ast\theta}(\theta_r, \phi_r)}^{-1} \circ u) [\sin(\theta) - \sin(\theta_r + \tau^{\ast\theta}(\theta_r, \phi_r))]| \\ & \leq C_h \|\tau\|_{\text{SO}(3)}. \end{aligned} \quad (70)$$

By further substituting (58), (65) and (70) into  $k_2(\theta_r, \phi_r, \rho_r, \theta_u, \phi_u)$ , we have

$$\begin{aligned} & |k_2(\theta_r, \phi_r, \rho_r, \theta_u, \phi_u)| \\ & \leq 2C_h \|\tau\|_{\text{SO}(3)} (1 + 2\|\nabla \tau\|_{\text{SO}(3)} + \|\nabla \tau\|_{\text{SO}(3)}^2) \leq 2C_h \epsilon + \mathcal{O}(\epsilon^2) \end{aligned} \quad (71)$$

where the conditions  $\|\tau\|_{\text{SO}(3)} \leq \epsilon$  and  $\|\nabla \tau\|_{\text{SO}(3)} \leq \epsilon$  are used in the last inequality.

By using (57) and (71), we bound the operator  $k(\theta_r, \phi_r, \rho_r, \theta_u, \phi_u)$  as

$$|k(\theta_r, \phi_r, \rho_r, \theta_u, \phi_u)| \leq 4C_h \epsilon + \mathcal{O}(\epsilon^2). \quad (72)$$

Therefore, we obtain

$$\frac{1}{8\pi^2} \int |k(\theta_r, \phi_r, \rho_r, \theta_u, \phi_u)| d\theta_r d\phi_r d\rho_r \leq 4C_h \epsilon + \mathcal{O}(\epsilon^2), \quad (73)$$

$$\frac{1}{2\pi^2} \int |k(\theta_r, \phi_r, \rho_r, \theta_u, \phi_u)| d\theta_u d\phi_u \leq 4C_h \epsilon + \mathcal{O}(\epsilon^2). \quad (74)$$

Then by using the Schur's Lemma, we have

$$\|H - H P_{\tau}^{\ast-1}\| \leq 4C_h \epsilon + \mathcal{O}(\epsilon^2). \quad (75)$$

Finally, by substituting (45) and (75) into (42) and the latter into (41),

$$\|H(x_{\tau}) - H(x)\|_{\text{SO}(3)} \leq \|H P_{\tau}^{\ast} - H\| \|\mathbf{x}\| \leq 8C_h \epsilon \|\mathbf{x}\| + \mathcal{O}(\epsilon^2)$$

we complete the proof.  $\square$

## APPENDIX D

## ROTATION EQUIVARIANCE OF SPHERICAL CNNs

*Proof of Proposition 2.* Without loss of generality, we consider multi-feature SCNN. From Proposition 1, we know that the rotation equivalence holds for spherical convolutions. Then at layer  $\ell$  of the SCNN, each spherical filter  $h_\ell^{fg}$  satisfies

$$H_\ell^{fg}(x_{(\ell-1)r}^g) = (H_\ell^{fg}(x_{\ell-1}^g))_r \quad (76)$$

for all  $f = 1, \dots, F_\ell$  and  $g = 1, \dots, F_{\ell-1}$ , where  $x_{(\ell-1)r}^g$ ,  $(H_\ell^{fg}(x_{\ell-1}^g))_r$  are rotated signals of  $x_{\ell-1}^g$ ,  $H_\ell^{fg}(x_{\ell-1}^g)$  by the rotation  $r$ . Since linear operations does not break the rotation equivariance, we have

$$\sum_{g=1}^F H_\ell^{fg}(x_{(\ell-1)r}^g) = \left( \sum_{g=1}^F H_\ell^{fg}(x_{\ell-1}^g) \right)_r. \quad (77)$$

Note that the pointwise nonlinearity  $\sigma(\cdot)$  applies to each element of the spherical signal  $x$  such that we have  $\sigma(r \circ x) = r \circ \sigma(x)$ . Thus, we further get

$$\sigma \left( \sum_{g=1}^F H_\ell^{fg}(x_{(\ell-1)r}^g) \right) = \left( \sigma \left( \sum_{g=1}^F H_\ell^{fg}(x_{\ell-1}^g) \right) \right)_r. \quad (78)$$

Since (78) holds at each layer  $\ell = 1, \dots, L$ , we conclude that the rotation equivariance holds for the SCNN.  $\square$

## APPENDIX E

## STABILITY OF SPHERICAL CNNs

We will need the following lemma that shows the propagation consequence of a spherical signal through the spherical convolution.

**Lemma 1.** *Let  $x \in \mathbb{L}^2(\mathbb{S}_2)$  be a spherical signal, and  $H$  be a Lipschitz filter with respect to  $C_h$  [cf. Def 4]. Then, it holds that*

$$\|H(x)\| \leq C_h \|x\|. \quad (79)$$

*Proof.* The spherical filter output is

$$\begin{aligned} H(x)(u) &= \frac{1}{8\pi^2} \int h(r_{\phi_r \theta_r \rho_r}^{-1} \circ u) x(\theta_r, \phi_r) \sin(\theta_r) d\theta_r d\phi_r d\rho_r \\ &= \frac{1}{8\pi^2} \int k(\theta_r, \phi_r, \rho_r, \theta_u, \phi_u) x(\theta_r, \phi_r) d\theta_r d\phi_r d\rho_r \end{aligned} \quad (80)$$

where  $k(\theta_r, \phi_r, \rho_r, \theta_u, \phi_u)$  is the operation kernel of the spherical convolution. Since  $|h(\theta_r, \phi_r)| \leq C_h$ , we have

$$\frac{1}{8\pi^2} \int |k(\theta_r, \phi_r, \rho_r, \theta_u, \phi_u)| d\theta_r d\phi_r d\rho_r \leq C_h, \quad (81)$$

$$\frac{1}{2\pi^2} \int |k(\theta_r, \phi_r, \rho_r, \theta_u, \phi_u)| d\theta_u d\phi_u \leq C_h \quad (82)$$

By using the Schur's Lemma in (53) and (54), we complete the proof  $\|H(x)\| \leq C_h \|x\|$ .  $\square$

*Proof of Theorem 2.* The Spherical CNN output is given by

$$\Phi(x; \mathcal{H}) = \sigma_L(H_L(x_{L-1})) = \sigma_L \left( \sum_{f=1}^F h_L^f *_{\text{SO}(3)} x_{L-1}^f \right). \quad (83)$$

We denote by  $H_L^f x_{L-1}^f = h_L^f *_{\text{SO}(3)} x_{L-1}^f$  and  $P_\tau x = x_\tau$  the concise notations of the spherical convolution and the perturbed signal for convenience of theoretical analysis. By using (83), the SCNN output difference induced by  $\tau$  is

$$\begin{aligned} \|\Phi(P_\tau x; \mathcal{H}) - \Phi(x; \mathcal{H})\| &= \left\| \sigma \left( \sum_{f=1}^F H_L^f \hat{x}_{L-1}^f \right) - \sigma \left( \sum_{f=1}^F H_L^f x_{L-1}^f \right) \right\| \\ &\leq C_\sigma \left\| \sum_{f=1}^F H_L^f \hat{x}_{L-1}^f - \sum_{f=1}^F H_L^f x_{L-1}^f \right\| \end{aligned} \quad (84)$$

where  $\hat{x}_{L-1}^f$  and  $x_{L-1}^f$  are the  $f$ th outputs of  $\Phi(P_\tau x; \mathcal{H})$  and  $\Phi(x; \mathcal{H})$  at  $(L-1)$ th layer, respectively. The last inequality is due to the Lipschitz property of the nonlinearity  $\sigma(\cdot)$ . Since the spherical convolution is linear, we get

$$\begin{aligned} \|\Phi(P_\tau x; \mathcal{H}) - \Phi(x; \mathcal{H})\| &\leq \sum_{f=1}^F C_\sigma \|H_L^f(\hat{x}_{L-1}^f - x_{L-1}^f)\| \\ &\leq C_\sigma C_h \sum_{f=1}^F \|\hat{x}_{L-1}^f - x_{L-1}^f\| \end{aligned} \quad (85)$$

where the first inequality is due to the triangle inequality and the second is obtained from Lemma 1. We observe a recursive process in (85) that the output difference at  $L$ th layer is upper bounded by the output difference at  $(L-1)$ th layer. By repeating this process, we have

$$\|\hat{x}_{L-1}^f - x_{L-1}^f\| \leq C_\sigma C_h \sum_{g=1}^F \|\hat{x}_{L-2}^g - x_{L-2}^g\|. \quad (86)$$

By substituting (86) into (85), we get

$$\|\Phi(P_\tau x; \mathcal{H}) - \Phi(x; \mathcal{H})\| \leq C_\sigma^2 C_h^2 F \sum_{g=1}^F \|\hat{x}_{L-2}^g - x_{L-2}^g\|. \quad (87)$$

By doing this recursively, we have

$$\begin{aligned} \|\Phi(P_\tau x; \mathcal{H}) - \Phi(x; \mathcal{H})\| &\leq C_\sigma C_h \sum_{f=1}^F \|\hat{x}_{L-1}^f - x_{L-1}^f\| \\ &\leq C_\sigma^{L-1} C_h^{L-1} F^{L-2} \sum_{g=1}^F \|\hat{x}_1^g - x_1^g\| \end{aligned} \quad (88)$$

where  $\hat{x}_1^g$  and  $x_1^g$  are the  $g$ th outputs of  $\Phi(P_\tau x; \mathcal{H})$  and  $\Phi(x; \mathcal{H})$  at 1st layer.

Now consider the term  $\|\hat{x}_1^g - x_1^g\|$ . According to the definitions of  $\hat{x}_1^g$  and  $x_1^g$ , their difference is

$$\|\hat{x}_1^g - x_1^g\| = \|\sigma(H_1^g P_\tau x) - \sigma(H_1^g x)\| \leq C_\sigma \|H_1^g P_\tau x - H_1^g x\| \quad (89)$$

where  $x$  is the input of the SCNN and the last inequality is due to the Lipschitz property of the nonlinearity. From Theorem 1, under the rotation distance we have

$$\|H_1^g P_\tau x - H_1^g x\|_{\text{SO}(3)} \leq 8C_h \epsilon \|x\| + \mathcal{O}(\epsilon^2). \quad (90)$$

Note that (90) holds for any spherical filter  $\{h_1^g\}_{g=1}^F$  at 1st layer. As such, by substituting (90) into (89), we get

$$\|\hat{x}_1^g - x_1^g\|_{\text{SO}(3)} \leq 8C_h C_\sigma \epsilon \|x\| + \mathcal{O}(\epsilon^2) \quad (91)$$

$\forall g = 1, \dots, F$ . By further substituting (91) into (88),

$$\|\Phi(P_\tau x; \mathcal{H}) - \Phi(x; \mathcal{H})\|_{\text{SO}(3)} \leq 8C_\sigma^L C_h^L F^{L-1} \epsilon \|x\| + \mathcal{O}(\epsilon^2)$$

we complete the proof.  $\square$

## REFERENCES

- [1] S. E. Reutebuch, H. Andersen, and R. J. McGaughey, "Light detection and ranging (lidar): an emerging tool for multiple resource inventory," *Journal of forestry*, vol. 103, no. 6, pp. 286–292, Sep. 2005.
- [2] A. Chang, A. Dai, T. Funkhouser, M. Halber, M. Niebner, M. Savva, S. Song, A. Zeng, and Y. Zhang, "Matterport3d: Learning from rgb-d data in indoor environments," in *5th International Conference on 3D Vision*, Qingdao, China, 10–12 Oct. 2017, pp. 667–676.
- [3] M. R. Dury, S. D. Woodward, S. B. Brown, and M. B. McCarthy, "Surface finish and 3d optical scanner measurement performance for precision engineering," in *30th Annual Meeting of the American Society for Precision Engineering*. Austin, TX: ASPE, 1–6 Nov. 2015, pp. 1–6.
- [4] K. Zhou, H. Bao, and J. Shi, "3d surface filtering using spherical harmonics," *Computer-Aided Design*, vol. 36, no. 4, pp. 363–375, 2004.
- [5] M. Yavartanoo, E. Y. Kim, and K. M. Lee, "Spnet: Deep 3d object classification and retrieval using stereographic projection," in *14th Asian Conference on Computer Vision*. Perth, Australia: Springer, 2–6 Dec. 2018, pp. 691–706.
- [6] A. Geiger, P. Lenz, C. Stiller, and R. Urtasun, "Vision meets robotics: The kitti dataset," *The International Journal of Robotics Research*, vol. 32, no. 11, pp. 1231–1237, 2013.
- [7] L. Maier-Hein, P. Mountney, A. Bartoli *et al.*, "Optical techniques for 3d surface reconstruction in computer-assisted laparoscopic surgery," *Medical image analysis*, vol. 17, no. 8, pp. 974–996, Dec. 2013.
- [8] F. J. Simons and A. Plattner, "Scalar and vector slepian functions, spherical signal estimation and spectral analysis," *arXiv preprint arXiv:1306.3184 [physics.data-an]*, 13 June 2013. [Online]. Available: <https://arxiv.org/abs/1306.3184>
- [9] E. Racah, C. Beckham, T. Maharaj, S. E. Kahou, M. Prabhat, and C. Pal, "Extremeweather: A large-scale climate dataset for semi-supervised detection, localization, and understanding of extreme weather events," in *31st Conference on Neural Information Processing Systems*. Long Beach, CA: Neural Inform. Process. Foundation, 4–9 Dec. 2017, pp. 3402–3413.
- [10] A. Makadia, L. Sorgi, and K. Daniilidis, "Rotation estimation from spherical images," in *17th International Conference on Pattern Recognition*. Cambridge, UK: IEEE, 26 Aug. 2004, pp. 590–593.
- [11] A. Makadia and K. Daniilidis, "Rotation recovery from spherical images without correspondences," *IEEE transactions on pattern analysis and machine intelligence*, vol. 28, no. 7, pp. 1170–1175, 2006.
- [12] I. M. Gelfand, R. A. Minlos, and Z. Y. Shapiro, *Representations of the Rotation and Lorentz Groups and their Applications*. Courier Dover Publications, 2018.
- [13] A. Derighetti, *Convolution operators on groups*. Springer, 2011.
- [14] A. Makadia and K. Daniilidis, "Spherical correlation of visual representations for 3d model retrieval," *International Journal of Computer Vision*, vol. 89, no. 2–3, pp. 193–210, 2010.
- [15] Y. Su and K. Grauman, "Learning spherical convolution for fast features from 360 imagery," in *31st Conference on Neural Information Processing Systems*. Long Beach, CA: Neural Inform. Process. Foundation, 4–9 Dec. 2017, pp. 529–539.
- [16] C. Esteves, C. Allen-Blanchette, A. Makadia, and K. Daniilidis, "Learning so(3) equivariant representations with spherical cnns," in *European Conference on Computer Vision*, Munich, Germany, 8–14 Sep. 2018, pp. 52–68.
- [17] T. S. Cohen, M. Geiger, J. Khler, and M. Welling, "Spherical cnns," in *6th International Conference on Learning Representations*, Vancouver, BC, 30 APR–3 MAY 2018.
- [18] D. E. Worrall, S. J. Garbin, D. Turmukhambetov, and G. J. Brostow, "Harmonic networks: Deep translation and rotation equivariance," in *30th Conference on Computer Vision and Pattern Recognition*. Hawaii, HO: IEEE, 22–25 July 2017, pp. 5028–5037.
- [19] B. S. Veeling, J. Linmans, J. Winkens, T. Cohen, and M. Welling, "Rotation equivariant cnns for digital pathology," in *21st International Conference on Medical image computing and computer-assisted intervention*, Granada, Spain, 16–20 Sep. 2018, pp. 210–218.
- [20] J. Li, Y. Bi, and G. H. Lee, "Discrete rotation equivariance for point cloud recognition," in *International Conference on Robotics and Automation*. Montreal, Canada: IEEE, 20–24 May 2019, pp. 7269–7275.
- [21] N. Perraudin, M. Defferrard, T. Kacprzak, and R. Sgier, "DeepSphere: Efficient spherical convolutional neural network with healpix sampling for cosmological applications," *Astronomy and Computing*, vol. 27, pp. 130–146, 2019.
- [22] M. Rosenthal, W. Wu, E. Klassen, and A. Srivastava, "Nonparametric spherical regression using diffeomorphic mappings," *arXiv:1702.00823v1 [stat.OT]*, 2 Feb. 2017. [Online]. Available: <http://arxiv.org/abs/1702.00823>
- [23] Z. Wu, S. Song, A. Khosla, F. Yu, L. Zhang, X. Tang, and J. Xiao, "3d shapenets: A deep representation for volumetric shapes," in *28th Conference on Computer Vision and Pattern Recognition*. Boston, MA: IEEE, 7–12 June 2015, pp. 1912–1920.
- [24] J. E. Mebius, "Derivation of the euler-rodrigues formula for three-dimensional rotations from the general formula for four-dimensional rotations," *arXiv preprint arXiv:math/0701759 [math.GM]*, 26 Jan. 2007. [Online]. Available: <https://arxiv.org/abs/math/0701759>
- [25] W. R. Scott, *Group theory*. Courier Corporation, 2012.
- [26] P. J. Kostelec and D. N. Rockmore, "Ffts on the rotation group," *Journal of Fourier analysis and applications*, vol. 14, no. 2, pp. 145–179, 2008.
- [27] J. R. Driscoll and D. M. Healy, "Computing fourier transforms and convolutions on the 2-sphere," *Advances in applied mathematics*, vol. 15, no. 2, pp. 202–250, 1994.
- [28] S. Mallat, "Group invariant scattering," *Communications on Pure and Applied Mathematics*, vol. 65, no. 10, pp. 1331–1398, Oct. 2012.
- [29] I. Goodfellow, Y. Bengio, and A. Courville, *Deep Learning*, ser. Adaptive Computation Mach. Learning Series. Cambridge, MA: The MIT Press, 2016.
- [30] A. Krizhevsky, I. Sutskever, and G. E. Hinton, "Imagenet classification with deep convolutional neural networks," in *26th Conference on Neural Information Processing Systems*. Harrahs and Harveys, Lake Tahoe: Neural Inform. Process. Foundation, 3–8 Dec. 2012, pp. 1097–1105.
- [31] B. Hu, Z. Lu, H. Li, and Q. Chen, "Convolutional neural network architectures for matching natural language sentences," in *28th Conference on Neural Information Processing Systems*. Montreal, CANADA: Neural Inform. Process. Foundation, 8–13 Dec. 2014, pp. 2042–2050.
- [32] H. Li, Z. Lin, X. Shen, J. Brandt, and G. Hua, "A convolutional neural network cascade for face detection," in *28th Conference on Computer Vision and Pattern Recognition*. Boston, MA: IEEE, 7–12 June 2015, pp. 5325–5334.
- [33] J. Bruna, W. Zaremba, A. Szlam, and Y. LeCun, "Spectral networks and deep locally connected networks on graphs," in *2nd International Conference on Learning Representations*, Banff, AB, 14–16 Apr. 2014, pp. 1–14.
- [34] M. Defferrard, X. Bresson, and P. Vandergheynst, "Convolutional neural networks on graphs with fast localized spectral filtering," in *30th Conference on Neural Information Processing Systems*. Barcelona, Spain: Neural Inform. Process. Foundation, 5–10 Dec. 2016, pp. 3844–3858.
- [35] F. Gama, A. G. Marques, G. Leus, and A. Ribeiro, "Convolutional neural network architectures for signals supported on graphs," *IEEE Transactions on Signal Processing*, vol. 67, no. 4, pp. 1034–1049, Feb. 2019.
- [36] S. Kurtsek, E. Klassen, Z. Ding, and A. Srivastava, "A novel riemannian framework for shape analysis of 3d objects," in *23rd Conference on Computer Vision and Pattern Recognition*. San Francisco, CA: IEEE, 13–18 June 2010, pp. 1625–1632.
- [37] O. C. Hamsici and A. M. Martinez, "Rotation invariant kernels and their application to shape analysis," *IEEE Transactions on Pattern Analysis and Machine Intelligence*, vol. 31, no. 11, pp. 1985–1999, 2008.
- [38] F. Gama, J. Bruna, and A. Ribeiro, "Stability properties of graph neural networks," *arXiv:1905.04497v5 [cs.LG]*, 23 Sep. 2020. [Online]. Available: <http://arxiv.org/abs/1905.04497>
- [39] K. Chen and L. Liu, "Geometric data perturbation for privacy preserving outsourced data mining," *Knowledge and information systems*, vol. 29, no. 3, pp. 657–695, 2011.
- [40] W. Huang, R. Wang, Y. Chen, H. Li, and S. Gan, "Damped multi-channel singular spectrum analysis for 3d random noise attenuation," *Geophysics*, vol. 81, no. 4, pp. V261–V270, 2016.
- [41] M. A. Nazari S., S. Gholtashi, A. R. Kahoo, W. Chen, and Y. Chen, "Data-driven multitask sparse dictionary learning for noise attenuation of 3d seismic data," *Geophysics*, vol. 82, no. 6, pp. V385–V396, 2017.
- [42] J. Schur, "Bemerkungen zur theorie der beschränkten bilinearformen mit unendlich vielen veränderlichen," *Journal für die reine und angewandte Mathematik (Crelles Journal)*, vol. 1911, no. 140, pp. 1–28, 1911.